

Quest for quantum advantage: Monte Carlo wave-function simulations of the Coherent Ising Machine

Manushan Thenabadu, Run Yan Teh, Jia Wang, Simon Kieseewetter, Margaret D Reid, Peter D Drummond
*Centre for Quantum Science and Technology Theory,
Swinburne University of Technology, Melbourne 3122, Australia*

The Coherent Ising Machine (CIM) is a quantum network of optical parametric oscillators (OPOs) intended to find ground states of the Ising model. This is an NP-hard problem, related to several important minimization problems, including the max-cut graph problem, and many similar problems. In order to enhance its potential performance, we analyze the coherent coupling strategy for the CIM in a highly quantum regime. To explore this limit we employ accurate numerical simulations. Due to the inherent complexity of the system, the maximum network size is limited. While master equation methods can be used, their scalability diminishes rapidly for larger systems. Instead, we use Monte Carlo wave-function methods, which scale as the wave-function dimension, and use large numbers of samples. These simulations involve Hilbert spaces exceeding 10^7 dimensions. To evaluate success probabilities, we use quadrature probabilities. We demonstrate the potential for quantum computational advantage through improved simulation times and success rates in a low-dissipation regime, by using quantum superpositions and time varying couplings to give enhanced quantum effects.

I. INTRODUCTION

Quantum computational advantage has been an important motivation for quantum computing researchers [1, 2]. The goal is to build a quantum device that solves problems faster than digital hardware. There are many recent experiments motivated by this goal [3–7]. However, the resulting data errors raise the issue that the device may not solve the original problem [8]. Additionally, a quantum computer with broadly useful applications is still not realized [9]. Here we study quantum advantage in practical optimization problems. We use the coherent Ising machine (CIM) as the computing architecture, since it targets such problems.

The CIM is intended to solve the Ising model ground state, initially developed to model phase transitions in magnetic materials [10]. The Ising model is a network of discrete spins $\sigma_k = \pm 1$ with nearest-neighbor interactions. More generally, we take into account arbitrary couplings J_{ij} and an external magnetic field h_j , at each site. The energy function of the model has the form,

$$E(\sigma) = -\sum_{i,j} J_{ij} \sigma_i \sigma_j - \sum_j h_j \sigma_j. \quad (1)$$

This has many applications to optimization problems across various fields, including computer science, medicine, logistics, finance, telecommunication and machine learning [11–13]. On mapping NP-hard and NP-complete problems to the Ising Hamiltonian [14, 15], one finds that the ground state corresponds to the optimal solution for these problems. Conventional computers face significant challenges in solving such complex optimization problems due to their exponential time complexity. In our study, the Ising model is mapped onto a quantum optical system, namely the coherent Ising Machine (CIM).

This computing architecture is inspired by the Ising model. It uses quantum mechanics to potentially over-

come these computational limitations, although it is not a universal, gate-based architecture. The CIM model comprises a network of Degenerate Optical Parametric Oscillators (DOPOs), where each DOPO element corresponds to an Ising spin. Coherent coupling between the DOPO elements is achieved using an optical delay line scheme [16]. In this scheme, DOPO pulses circulate within an optical ring cavity, with each pulse representing an Ising spin. The phase of the pulse determines whether it is in the spin-up or spin-down state.

To implement the J_{ij} coupling between DOPO pulses, a portion of each pulse in the optical ring is picked off and fed through an optical phase-sensitive amplifier (PSA), followed by delay lines equipped with intensity and phase modulators. This setup allows for arbitrary coupling between any two pulses within the system, determined by the coupling coefficient J_{ji} . A small-scale DOPO network was first experimentally realized by Marandi et al. [17], using a time-division multiplexing scheme within a single ring resonator, with spin-spin interactions implemented through mutual injections of DOPO pulses using delay interferometers. Since then, large-scale networks comprising over 10^4 DOPOs [18–20] have been investigated, although these use an incoherent measurement feedback (MFB) strategy.

To simulate the quantum dynamics of such parametric systems, master equation methods could be used [21], but these scale quadratically in the Hilbert space dimension, making them rapidly impractical for larger systems with many coupled oscillators. Positive-P phase-space methods [22, 23] are useful for the present experimental parameters, and are scalable, but this method has challenges in highly quantum regimes due to sampling errors. A third approach used for MFB simulations [24], the Gaussian approximation, is inapplicable when there are non-Gaussian quantum superposition states. In this study, we employ Monte Carlo wave-function (MCWF) methods [25], which scale linearly in the Hilbert space

dimension, and can treat any quantum state. We report on simulations that exceed 10^7 Hilbert dimensions. Although our simulations are still in the small mode limit of $M < 6$, they are beyond the reach of master equations, and can treat extreme quantum regimes.

We investigate several problems, ranging from anti-ferromagnetic frustrated problems to max-cut graph problems. We evaluate the success rate through an x -quadrature measurement of the DOPO outputs. The success rate is calculated from joint probabilities of quadratures $P(x_1, x_2, \dots, x_m)$, with $x_i \geq 0$ as positive spin and $x_i < 0$ as negative spin. We investigate multiple strategies for initial quantum state, while dynamically changing the coupling strength and other parameters, to improve the success rate of the simulations. We find a speed up in performance and improved success rates with nonclassical initial states.

Because an accurate simulation of this type of computer is even harder than the Ising problem, our conclusions are only indicative. Small-scale devices that we can simulate cannot solve large Ising problems. Nevertheless, we can investigate whether quantum superpositions have a potential for quantum advantage. We find evidence for more rapid convergence to a solution when quantum superpositions are present. We also show that a clear limitation of this architecture is decoherence due to absorption in the spin couplings. This indicates that other, more coherent couplings may be beneficial.

II. HAMILTONIAN AND MASTER EQUATION

We first consider a single DOPO. This represents a single Ising spin with spin up or spin down configurations, given by the Hamiltonian [26, 27],

$$H/\hbar = \sum_{i=1}^2 \left(\omega_i a_i^\dagger a_i + a_i^\dagger \Gamma_i + a_i \Gamma_i^\dagger \right) + \frac{i\bar{g}}{2} \left(a_2 a_1^{\dagger 2} - a_2^\dagger a_1^2 \right) + i\epsilon \left(a_2^\dagger e^{-i\omega_2 t} - a_2 e^{i\omega_2 t} \right). \quad (2)$$

Here a_2 is the pump mode, a_1 is the signal/idler mode, ω_2 and ω_1 are the pump and signal mode frequencies, and \bar{g} is the coupling strength between the optical cavity modes. The first term represents the free evolution and linear damping of the optical cavity modes, the second term is the coupling between the pump and signal modes, and the third term represents the driving of the pump mode by an external field of amplitude ϵ with frequency ω_2 .

When the pump mode decay rate is much larger than the signal mode decay rate ($\gamma_2 \gg \gamma_1$), the pump mode can be eliminated through adiabatic elimination [28, 29]. The simpler Hamiltonian that results reads,

$$H = \hbar \bar{\Delta} a^\dagger a + i\hbar \lambda (a^{\dagger 2} - a^2) + \gamma \left(a^\dagger \Gamma_1 + a \Gamma_1^\dagger \right) + \frac{g^2}{2} \left(a^2 \Gamma_2^\dagger + a^{\dagger 2} \Gamma_2 \right), \quad (3)$$

where a is the signal mode of the DOPO and Γ_1, Γ_2 are the reservoir modes. Here $\bar{\Delta} = \omega_1 - \omega_2/2$ is the detuning, λ the pump driving strength and g is the dimensionless two-photon dissipation rate and γ single photon dissipation rate, where:

$$\lambda = \frac{|\bar{g}\epsilon|}{\gamma_1 \gamma_2} \\ g = \sqrt{\frac{\bar{g}^2}{2\gamma_1 \gamma_2}}. \quad (4)$$

Initially, we set $\gamma = 1$ to determine the time-scale, and define a characteristic coherent amplitude of

$$\alpha = \frac{\sqrt{\lambda}}{g}. \quad (5)$$

The steady state is known exactly [27], and it is approximately a mixture of coherent states $|\pm\alpha\rangle$. This gives a characteristic photon number scale of $n_c = |\alpha|^2$. Prior to this, the dynamical behavior in highly quantum regimes with $g \gtrsim 1$ [30–32] leads to an approximate transient Schrödinger cat state:

$$|\Psi_C\rangle = N_C [|\alpha\rangle + |-\alpha\rangle], \quad (6)$$

which later decays to the impure steady state from decoherence caused by the single photon decays.

The following master equation is applicable to a CIM of M coherently coupled oscillators [33–35]:

$$\frac{\partial \rho}{\partial t} = \sum_i \left\{ -\Delta_i [a_i^\dagger a_i, \rho] + \frac{\lambda}{2} [a_i^\dagger a_i^\dagger - a_i a_i, \rho] \right\} + \sum_i \left\{ \gamma \left(2a_i \rho a_i^\dagger - a_i^\dagger a_i \rho - \rho a_i^\dagger a_i \right) \right\} + \sum_i \left\{ \frac{g^2}{2} \left(2a_i^2 \rho a_i^{\dagger 2} - a_i^{\dagger 2} a_i^2 \rho - \rho a_i^{\dagger 2} a_i^2 \right) \right\} + \sum_{i,j} \frac{|J_{ij}|}{2} \left(2L_{ij} \rho L_{ij}^\dagger - L_{ij}^\dagger L_{ij} \rho - \rho L_{ij}^\dagger L_{ij} \right), \quad (7)$$

with the usual notation that a_i is the annihilation operator for mode i with $i = 1, \dots, M$, Δ_i is the detuning for the i^{th} mode (here, we set $\Delta_i = 0$), λ is the pump strength, and γ and g are the one photon and two photon dissipative rates, respectively. The coherent coupling is given by the last term of the above equation, where the J matrix describes the coupling strength between the modes with $J_{ij} = J_{ji}$ and we set $J_{ii} = J_{jj} = 0$. The operators L_{ij} are the Lindblad operators for the couplings, defined as $L_{ij} = a_i - \frac{J_{ij}}{|J_{ij}|} a_j$. If the signs are the same throughout, the sign of J_{ij} distinguishes the ferromagnetic case (+), in which the spins are aligned, from the anti-ferromagnetic (-) case.

In the classical limit, the corresponding mean-field equation is [35, 36]:

$$\dot{\alpha}_i = -\gamma \alpha_i + \sum_k (J_{ik} \alpha_k - |J_{ik}| \alpha_i) + \alpha_i^* (\lambda - g^2 \alpha_i^2). \quad (8)$$

This is known to provide a route to finding the Ising ground state, apart from issues with solutions being trapped in non-extremal states. Here, we consider the full quantum problem, and investigate conditions for finding the solution in regimes where the mean-field equations are no longer applicable, due to strong entanglement and quantum noise effects.

A. Quantum jump method

In this work, we investigate using the Coherent Ising Machine (CIM) model to solve combinatorial optimization problems in highly quantum regimes. Although algorithms exist that can solve the Ising model with more than 100 spins [37], conventional computers struggle with larger numbers of spins due to the exponential time complexity. A CIM model with a quantum architecture may offer advantages in performance speed and energy efficiency compared to its classical counterpart [38]. In this study, we map our Ising model to an optical quantum system and evaluate the system dynamics by utilizing the full Hilbert space, except for a number cut-off. For the system evolution, continuous methods exist [39–41] as another alternative. Here, we employ the Monte Carlo Wave Function (MCWF) method in our numerical simulations of the CIM to assess the system dynamics.

Let the wave-function of the system at time t be a normalized state $|\psi(t)\rangle$. Using the MCWF method, the system's evolution is governed by the Schrödinger equation with a non-Hermitian effective Hamiltonian:

$$H_{eff} = H_{sys} - \frac{i\hbar}{2} \sum_n C_n^\dagger C_n, \quad (9)$$

where the first term consists of the system's Hermitian part of the Hamiltonian Eq. 3, $H_{sys} = \hbar\Delta a^\dagger a + i\hbar\frac{\lambda}{2}(a^{\dagger 2} - a^2)$ and the second term represents non-Hermitian terms (often referred to as Lindblad terms in other methods), including dissipation and coupling, expressed by the jump operators C_n .

We then calculate the wave-function $|\psi^{(1)}(t + \delta t)\rangle$ by evolving $|\psi(t)\rangle$ under the above non-Hermitian Hamiltonian H_{eff} :

$$|\psi^{(1)}(t + \delta t)\rangle = \left(1 - \frac{i\delta t}{\hbar} H_{eff}\right) |\psi(t)\rangle. \quad (10)$$

Here δt must be sufficiently small, allowing us to ignore higher-order terms δt^2 and above. We use a slightly modified version of the original algorithm proposed by M̃zlmer et al. [42], where time integration is performed using a 4th-order Runge-Kutta method. Next, we evaluate the square of the norm:

$$\begin{aligned} |norm|^2 &= \langle \psi^{(1)}(t + \delta t) | \psi^{(1)}(t + \delta t) \rangle \\ &= \langle \psi(t) | \left(1 + \frac{i\delta t}{\hbar} H_{eff}^\dagger\right) \left(1 - \frac{i\delta t}{\hbar} H_{eff}\right) | \psi(t) \rangle \\ &= 1 - \delta p. \end{aligned} \quad (11)$$

Since the evolution occurs under a non-Hermitian Hamiltonian H_{eff} , the norm of the wave-function decreases by δp . We integrate the system until a certain threshold, determined by a uniformly distributed random number ϵ , is reached. Once this threshold is met, a quantum jump occurs, and the system evolves according to one of the collapse operators, projecting the state $|\psi(t)\rangle$ using the collapse operator C_n :

$$|\psi^{(1)}(t + \delta t)\rangle = \frac{C_n |\psi(t)\rangle}{\langle \psi(t) | C_n^\dagger C_n | \psi(t) \rangle^{1/2}}. \quad (12)$$

When multiple collapse operators are present, another random number r is generated to select which collapse operator causes the jump. The jump occurs when the following inequality is satisfied:

$$\sum_{i=1}^n P_i \geq r, \quad (13)$$

where n is the smallest integer that satisfies the inequality, and $P_i = \langle \psi(t) | C_n^\dagger C_n | \psi(t) \rangle / \delta p$.

B. Success Rate measurement

We wish to evaluate the success rate, which represents the probability of measuring the system in the optimal solution. This requires calculating the joint probabilities $P(x_1, x_2, \dots, x_M)$ of the quadrature measurements, where $x_i \geq 0$ corresponds to spin-up and $x_i < 0$ corresponds to spin-down for the i^{th} mode, with M modes.

First, we consider the simulation to be described by the single-mode density matrix $\rho = |\psi\rangle\langle\psi|$. The density matrix can also be expanded in the number basis as:

$$\rho = \sum_{n,m} \rho_{nm} |n\rangle\langle m|. \quad (14)$$

The x -quadrature probability distribution can be computed from the density matrix ρ , expanded in the number state basis, as:

$$\langle x | \rho | x \rangle = \sum_{n,m} \rho_{nm} \langle x | n \rangle \langle m | x \rangle. \quad (15)$$

Similarly, if we expand the density matrix in terms of the wave-function ψ , we get:

$$|\langle \psi | x \rangle|^2 = \sum_{n,m} \psi_{nm} |n\rangle\langle m|, \quad (16)$$

where $\psi_{nm} = \Psi_n \otimes \Psi_m$ are the coefficients of the number state expansion, with a photon cutoff of N . By plotting the diagonal elements of $\langle x | \rho | x \rangle$, we can evaluate the probability density $P(x)$ of the x -quadrature measurement.

Next, we calculate the joint probability distribution for the quadrature measurement of a DOPO with M

modes as:

$$P(x_1, x_2 \dots x_M) = |\langle \psi | x_1, x_2 \dots x_M \rangle|^2 \\ = \sum_{\mathbf{m}} \sum_{\mathbf{m}'} \psi_{\mathbf{m}, \mathbf{m}'} \prod_{i=1}^M \langle m_i | x_i \rangle \langle x_i | m'_i \rangle. \quad (17)$$

Here $\mathbf{m} = [m_1, m_2, \dots, m_M]$ and $\mathbf{m}' = [m'_1, m'_2, \dots, m'_M]$. To evaluate the success rate from the joint probabilities $P(x_1, x_2 \dots x_M)$, we integrate over the quadratures:

$$\int_{x_1} \int_{x_2} \dots \int_{x_M} P(x_1, x_2 \dots x_M) dx_1 dx_2 \dots dx_M. \quad (18)$$

This can be written as:

$$\sum_{\mathbf{m}} \sum_{\mathbf{m}'} \psi_{\mathbf{m}, \mathbf{m}'} \prod_{i=1}^M \int_{x_i} \langle m_i | x_i \rangle \langle x_i | m'_i \rangle dx_i \\ = \sum_{\mathbf{m}} \sum_{\mathbf{m}'} \psi_{\mathbf{m}, \mathbf{m}'} \Lambda^{(\sigma_1)}(m_1, m'_1) \otimes \Lambda^{(\sigma_2)}(m_2, m'_2) \dots \\ \otimes \Lambda^{(\sigma_M)}(m_M, m'_M). \quad (19) \quad (20)$$

In this expression, $\Lambda(m_i, m'_i)$ are the Hermite integrals for the i^{th} mode, evaluated analytically as:

$$\Lambda(m_i, m'_i) = \int H_{m_i}(x) H_{m'_i}(x) dx, \quad (21)$$

where σ_i represents the spin for the i^{th} mode. On binning the quadrature measurements for two possible spins, we have $\sigma_i = \{+, -\}$ depending on the spin of each mode. Hence,

$$\Lambda^+(m_i, m'_i) = \int_0^{\infty} H_{m_i}(x) H_{m'_i}(x) dx, \\ \Lambda^-(m_i, m'_i) = \int_{-\infty}^0 H_{m_i}(x) H_{m'_i}(x) dx. \quad (22)$$

We evaluate these integrals using standard Gaussian integrals:

$$\int_0^{\infty} x^n e^{-x^2} dx = \frac{\Gamma(\frac{n+1}{2})}{2} \\ \int_{-\infty}^0 x^n e^{-x^2} dx = (-1)^n \frac{\Gamma(\frac{n+1}{2})}{2} \quad (23)$$

The Gamma function $\Gamma(\frac{n+1}{2})$ can be expressed in terms of factorials as:

$$\Gamma\left(\frac{2n+1}{2}\right) = \frac{(2n)!}{4^n n!} \sqrt{\pi} \quad (24)$$

Thus, the Hermite integrals $\Lambda^{\pm}(m_i, m'_i)$ can be rewritten in the form:

$$\frac{m_i! m'_i!}{2} \sum_{p,l=0}^{\lfloor \frac{m_i}{2} \rfloor} (\pm)^{m+n-2p-2l} (-1)^{p+l} \frac{(m_i + m'_i - 2p - 2l)!}{p!(m_i - 2p)!!(m'_i - 2l)! \left(\frac{m_i + m'_i - 2p - 2l}{2}\right)!} \quad (25)$$

where $\lfloor \frac{m_i}{2} \rfloor$ indicates the floor function, rounding down the value of $\frac{m_i}{2}$. When measuring the success rate of our simulations using Eq. 19, we utilize the tensor identity $(A \otimes B \otimes \dots) = (A \otimes I \otimes \dots) (I \otimes B \otimes \dots) \dots$, allowing the algorithm to scale efficiently with the wavefunction. To implement the simulations, we developed two separate codes to allow cross-checking. One is in MATLAB using the xSPDE4 library [43], and another in Python utilizing the QuTiP library [44, 45].

C. Purity Calculation

We can calculate the quantum purity in our simulation as a means of determining the effects of decoherence of the initial quantum state. The sampled purity of the conditional density matrix ρ can be evaluated from the sampled trajectory wave-functions $|\psi_i\rangle$, as given by:

$$\rho = \frac{1}{N_t} \sum_{i=1}^{N_t} |\psi_i\rangle \langle \psi_i|, \quad (26)$$

where N_t is the number of trajectories. The squared density matrix ρ^2 is:

$$\rho^2 = \frac{1}{N_t^2} \sum_{i,j=1}^{N_t} |\psi_i\rangle \langle \psi_i | \psi_j\rangle \langle \psi_j|, \quad (27)$$

Defining $|\psi_i\rangle \langle \psi_i| = \sum_{n,m} \rho_{nm}^{(i)} |n\rangle \langle m|$, the purity is given by the trace of ρ^2 , expressed as:

$$Tr(\rho^2) = \frac{1}{N_t^2} \sum_{i,j=1}^{N_t} \sum_{n,m=1}^{N_c^M} \rho_{nm}^{(i)} \rho_{mn}^{(j)}. \quad (28)$$

Here N_c is the cut off, M is the number of modes and $\rho_{nm}^{(i)}$ are the i -th density matrix elements. In evaluating the summation in $Tr(\rho^2)$, the indices n and m run over $n = m = 1, 2, \dots, N_c^M$.

III. FIXED PARAMETER SIMULATIONS

In the simulations, we consider the detuning $\bar{\Delta}$ to be negligible and initially set the linear dissipation coefficient γ to unity. This allows us to scale all parameters with respect to the signal mode single-photon decay rate γ , which gives a dimensionless simulation time-scale γt . In this section, we focus on simulations with fixed parameters. The following section investigates dynamical, time-varying parameters which can vary throughout the passage to the final, measured state.

A. Initial quantum states

The initial state of our simulation should ideally encompass all possible solutions, meaning that at the beginning, for a system with M modes and a particular

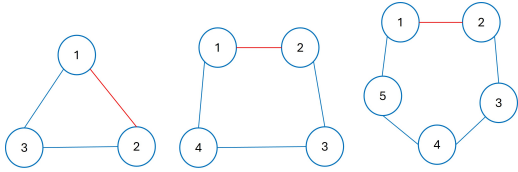


Figure 1: Ising spin diagram of $M = 3$, $M = 4$ and $M = 5$ spin arrangements with nearest neighbor interactions only, with uniform interaction strength ($J_{ij} = -1$, where i and j are nearest neighbor modes), with the sign of the J_{12} interaction flipped ($J_{12} = J_{21} = 1$).

spin configuration, the success rate would be $\sim \frac{1}{2^M}$. An important issue is the cut-off $N_c > n_c$, which largely determines how many modes can be treated. For good accuracy, this must be large enough so that errors due to number truncation are negligible. Yet, if the average photon number n_c is too low, the quantum noise causes prohibitive errors in detecting the output quadrature sign.

A vacuum state in all modes $\psi_{vac} = |0\rangle^{\otimes M}$ is the simplest to generate experimentally. This can evolve to any solution at later times. It is also the most classical state that we study, which serves as a benchmark in our simulations. One of the ways we investigate the influence of quantum effects is by initializing the simulation with a more non-classical state. The motivation is to explore whether such a state can influence the simulation's performance. In particular, we treat highly entangled initial cat states, under the assumption that these extremely non-classical states may provide evidence of any quantum advantage.

We consider two alternative initial quantum states: the first is an outer product of cat states equivalent to all 2^M spin states,

$$\psi_{sup} = \mathcal{N}_c^M (|\alpha\rangle + |-\alpha\rangle)^{\otimes M} \quad (29)$$

with coherent amplitude α . The second state is an M -partite entangled state:

$$\begin{aligned} \psi_{ent} = \mathcal{N}_M \{ & (|\alpha\rangle + |-\alpha\rangle)_1 |0\rangle_2 \dots |0\rangle_M \\ & + |0\rangle_1 (|\alpha\rangle + |-\alpha\rangle)_2 \dots |0\rangle_M + \dots \\ & + |0\rangle_1 |0\rangle_2 \dots (|\alpha\rangle + |-\alpha\rangle)_M \} \end{aligned} \quad (30)$$

where \mathcal{N}_M is the normalization factor. This is a quantum superposition, but with only one mode initialized to a cat state. The rationale for using ψ_{sup} and ψ_{ent} , is to investigate whether introducing quantum superposition and entanglement at the start of the simulation improves the CIM performance compared to the classical vacuum state ψ_{vac} .

B. Case I: Frustrated problems

We first consider a simple case of anti-ferromagnetic Ising spins ($J_{ij} < 0$), where neighboring anti-parallel

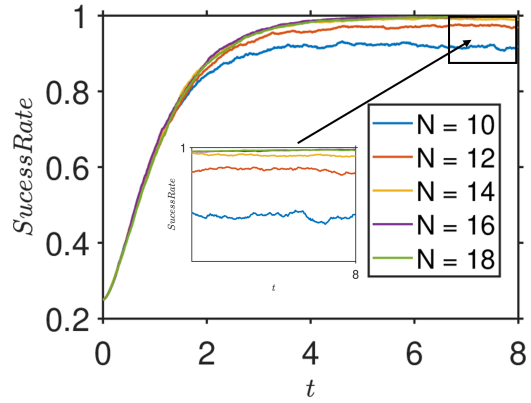


Figure 2: Success rate variation with varying photon cut-off N . Simulation parameters are set to $\lambda = 2.4$ and $g = 0.6$. Here the couplings J_{ij} are as in the $M = 3$ case in Fig (1), with ψ_{vac} as the initial state.

spins result in the lowest energy with uniform interaction strength $|J_{ij}|$ (the same for all $i \neq j$) and $J_{ij} = 0$ when $i = j$. We examine three cases as in figure 1. The first involves spins arranged in a triangle ($M = 3$), the second involves spins arranged in a square ($M = 4$), and the third involves spins arranged in a pentagon ($M = 5$).

In the first case, the energy is minimized when each spin is aligned opposite to its neighbors. We take $J_{ij} = -1$, where i and j are nearest neighbor modes. After the first two spins are aligned oppositely, the third spin becomes *frustrated* due to two possible configurations that provide the same low energy. This simultaneous minimization with respect to the other two spins leads to a six-fold degeneracy. In this study, we flip the sign of J_{12} ($J_{12} = J_{21} = 1$) interaction, thereby reducing the degeneracy to two.

We simulate the system starting from the initial vacuum state ψ_{vac} and, for comparison purposes, benchmark it against the initial states ψ_{sup} and ψ_{ent} , as defined by Eqs. 29 and 30. Throughout our simulations, we fix $\alpha = 2.582$, which results in a mean photon number of 6.667 at steady state. Due to computational memory limitations, we select a photon cutoff of $N = 16$, including the state $|0\rangle$. This is appropriate as it is three standard deviations from the mean photon number. The suitability of this cutoff is illustrated in Figure [2], where we vary N in the simulation to assess information loss, represented here by the success rate.

C. Case II: 4-mode frustrated problem

We next consider a 4-mode coupling matrix

$$J = \begin{bmatrix} 0 & J_{12} & -0.4 & -0.2 \\ J_{21} & 0 & -0.2 & -0.1 \\ -0.4 & -0.2 & 0 & -0.1 \\ -0.2 & -0.1 & -0.1 & 0 \end{bmatrix}, \quad (31)$$

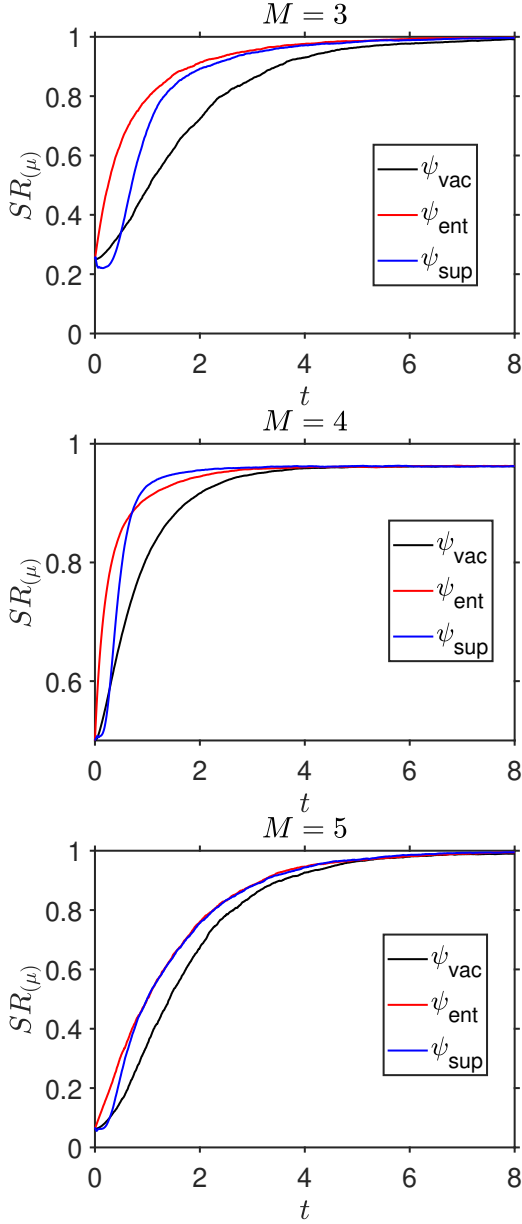


Figure 3: Evolution of the success rate for the anti-ferromagnetic spin problem for three cases, $M = 3$, $M = 4$ and $M = 5$. Three initial states are compared: the vacuum state ψ_{vac} (Black), the coherent superposition state ψ_{sup} (Blue) and the M -partite entangled state ψ_{ent} (red). Simulation parameters are set to $\lambda = 2.4$ and $g = 0.6$, with a total simulation time of $t = 8$ and $N_{steps} = 1200$ time steps, averaged over 10^4 realizations. Here J_{ij} values are given in 1.

where J_{12} is positive. When J_{12} is slightly less than 0.3, a conventional CIM often fails to find the ground state. Here, we take the specific value $J_{12} = 0.295$.

We simulated a 4-mode CIM with the coupling matrix Eq. (31), with the single-photon decay rate $\gamma = 1$, the two-photon decay rate $g = 0.75$, and a pump amplitude $\lambda = 1.125$. The total dimensionless simulation

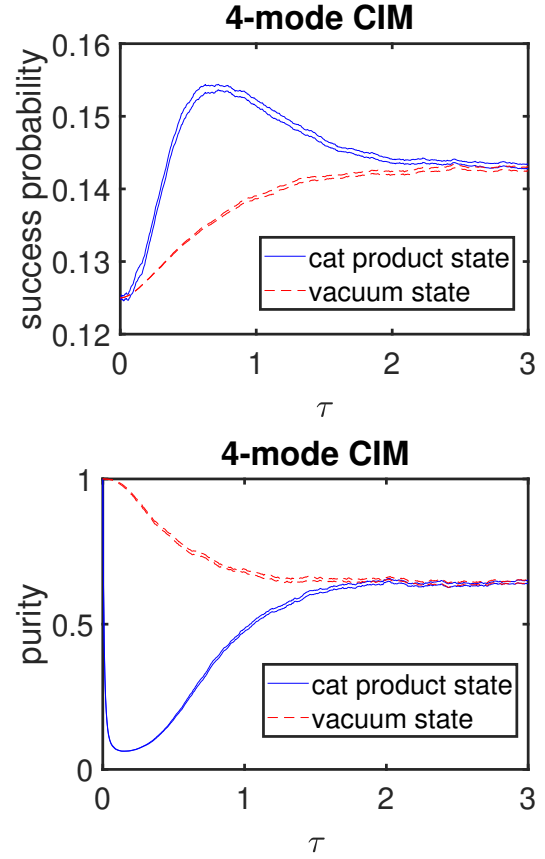


Figure 4: The time evolution of the success probability (top figure) and the purity (bottom figure), for different initial states, the vacuum state and a cat product state. The coupling matrix is given by Eq. (31), with $J_{12} = 0.295$. The single-photon decay rate is $\gamma = 1$, the two-photon decay rate is $g = 0.75$, and a pump amplitude is $\lambda = 1.125$. The total dimensionless simulation time is $T = 3$, with 10^4 samples and 600 time steps. A photon cutoff number of 5 is chosen. The two lines in each case indicate the sampling error.

time is $T = 3$, with 10^4 samples and 600 time steps. The steady state amplitude $|\alpha|$ is determined by the relation $\alpha^2 = \lambda/g^2$, which is $|\alpha| = \sqrt{2}$ for the parameters used here. Because of this small $|\alpha|$ amplitude, a small photon number cutoff of 5 was chosen.

The time evolution of the success rate and purity are computed for two different initial states, namely the vacuum state and a cat product state Eq. (29) with the number of modes, $M = 4$. These results are presented in Fig. 4.

The time step and sampling errors are estimated by xSPDE4. For the initial vacuum state simulation, the RMS relative time-step error is less than 3×10^{-4} and the sampling error is $\sim 4 \times 10^{-3}$. For the initial cat product state simulation, the time-step error is about 10 times larger while the sampling error is almost identical.

The results, shown in Fig (4) show that while the suc-

cess probability is relatively low, which is partially due to the low photon number and large quantum fluctuations, there is a strong transient enhancement in the success rate when using a quantum Schrödinger cat initial state. However, the initial purity is degraded. The pure initial quantum state is rapidly transformed into a mixture, in a similar way to the decoherence of Schrödinger cat states in a damped harmonic or parametric oscillator [30, 46].

We conclude from this that a static parameter approach is not optimal, for two reasons. Firstly, using a relatively low photon number in the final readout state causes large uncertainties in the readout sign, from quantum noise. Secondly, while some classical damping is essential in order to obtain a stable final state, it also leads to a rapid loss in purity owing to the resulting decoherence.

IV. DYNAMICAL STRATEGIES AND PURITY

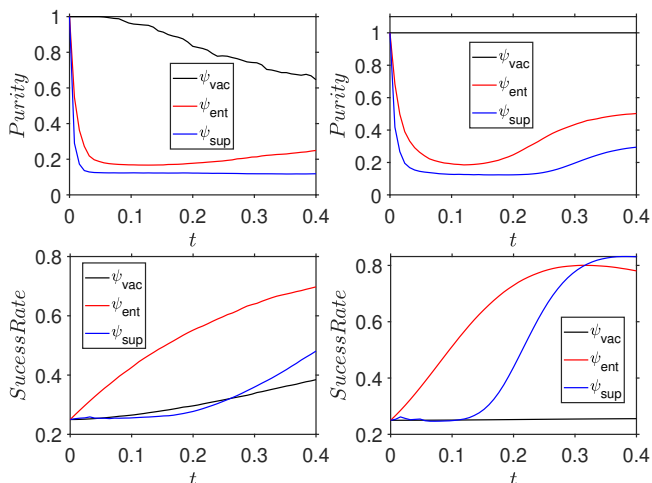
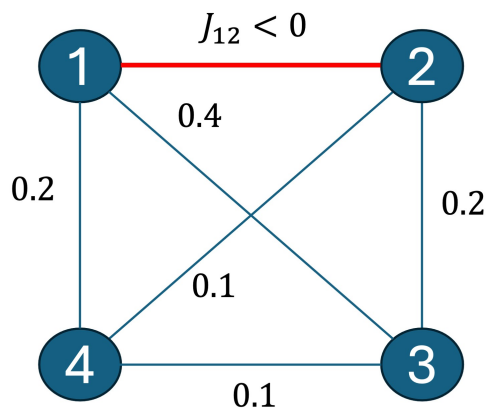
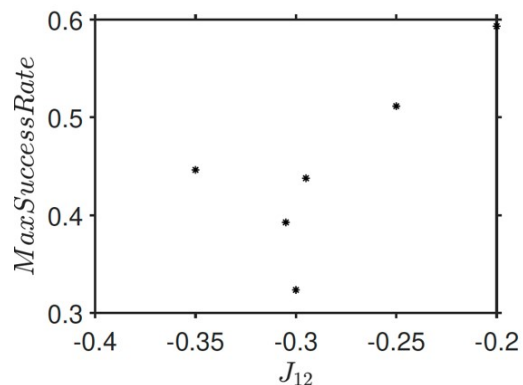


Figure 5: (a) Investigating the impact of initial states on purity and success rate for $M = 3$ case in Fig (1), with varying initial states in the short time scale. Top Plots: Purity and Bottom Plots: Corresponding Success rates. Here we consider two settings, Left Plots: with high-quantum noise setting ($g = 0.6$, $\gamma = 1$) and Right Plots: low-quantum noise setting ($g = 0.1$, $\gamma(t) = t/t_{max}$ and $J_{coef}(t) = 3t/t_{max} + 1$), with simulation time of $t_{max} = 0.4$ with $t_{steps} = 50$ using 10^3 trajectories.

From Figure 3, we observe an improvement in performance for all cases ($M = 3$, $M = 4$ and $M = 5$), when a non-classical state is used at the start of the simulation. Although the coherent superposition state ψ_{sup} performs poorly initially, it eventually surpasses the initial vacuum state ψ_{vac} simulation and even the M -partite entangled state ψ_{ent} in the $M = 4$ case. This suggests that both entanglement and superposition may contribute to enhancing the performance of the coherent



(a)



(b)

Figure 6: a: Ferromagnetic spin problem with specialized weights. b: Maximum Success rate for different J_{12} in (a).

Ising machine (CIM). For the $M = 5$ case, in Figure 3, however, the performance improvement is marginal. To understand this we look at an additional measurement, which is the purity, introduced in section II (C).

The results presented in Figure 3 are simulated in a high-quantum-noise regime with large dissipation ($g = 0.6$ and $\gamma = 1$), where many damping terms contribute to the master equation Eq. 7. In such a regime, starting with a highly quantum state is not beneficial as it decoheres very quickly. This is evident from the left plots in Figure 5 where the highly quantum states ψ_{ent} and ψ_{sup} lose purity at a greater rate compared to starting with a more classical state like ψ_{vac} state.

To preserve the purity for a longer duration, it is advantageous for starting the highly quantum state in a low-quantum-noise environment. While the coupling term in Eq. 7 appears to dampen some modes, increasing the coupling between the DOPOs is more beneficial in the low-quantum-noise setting when starting with a highly quantum state. We will treat non-decoherent couplings elsewhere.

However, as shown in bottom right plot in Figure 5,

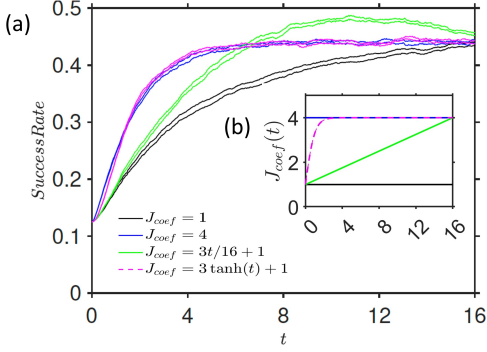


Figure 7: a: Time evolution of the success rate for the special ferromagnetic problem, with alternate strategies for the interaction coefficient J_{coef} . b: Increasing J_{coef} from $J_{coef} = 1$ to $J_{coef} = 4$ using three different strategies: constant (blue), a linear increase (green), and a hyperbolic tangent function to emulate a rapid initial increase (purple).

the improved performance in the low-noise environment is short-lived. Over longer time scales, quantum noise becomes essential to stabilize the steady state, even when starting with a highly quantum state.

Next, we consider a weighted ferromagnetic problem, as illustrated in Figure 6, where we flip the sign of J_{12} before. Here we vary J_{12} , and observe a reduction in the maximum success rate when $J_{12} \sim -0.3$, as shown in Figure 6 (b). We conduct simulations around $J_{12} \sim -0.3$. The reduction in success rate is primarily due to near-optimal solutions having an Ising energy close to the optimal solution at $J_{12} \sim -0.3$. At $J_{12} = -0.3$, we observe a fourfold degeneracy; thus, we choose $J_{12} = -0.295$, which reduces the degeneracy to two.

We perform simulations while keeping the initial state fixed as $\psi_{vac} = |0\rangle^{\otimes M}$ and vary the interaction strength by multiplying J_{ij} by a time-dependent interaction coefficient $J_{coef}(t)$. Now the master equation in Eq. 7 reads

$$\begin{aligned} \frac{\partial \rho}{\partial t} = & \sum_i \left\{ -\Delta_i [a_i^\dagger a_i, \rho_i] + \frac{\lambda}{2} [a_i^\dagger a_i^\dagger - a_i a_i, \rho] \right\} \\ & + \sum_i \left\{ \gamma (2a_i \rho a_i^\dagger - a_i^\dagger a_i \rho - \rho a_i^\dagger a_i) \right\} \\ & + \sum_i \left\{ \frac{g^2}{2} (2a_i^2 \rho a_i^{\dagger 2} - a_i^{\dagger 2} a_i^2 \rho - \rho a_i^{\dagger 2} a_i^2) \right\} \\ & + \sum_{i,j} J_{coef}(t) \frac{|J_{ij}|}{2} (2L_{ij} \rho L_{ij}^\dagger - L_{ij}^\dagger L_{ij} \rho - \rho L_{ij}^\dagger L_{ij}), \end{aligned} \quad (32)$$

The coefficient $J_{coef}(t)$ is used to increase the interaction strength by four times. Different strategies for increasing $J_{coef}(t)$ are shown in Figure 7(b). Increasing $J_{coef}(t)$ enhances the interaction between the DOPO elements, thereby increasing entanglement in the system.

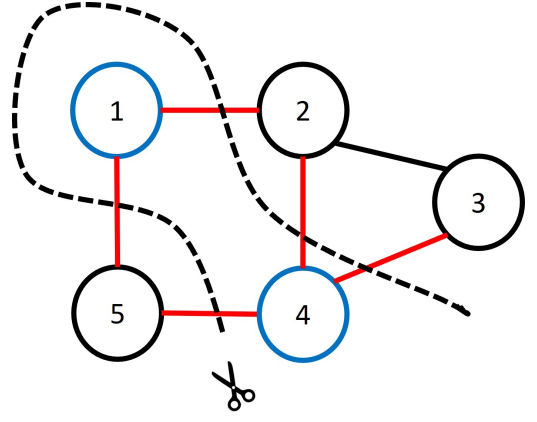


Figure 8: Spin diagram of a Max-cut graph problem depicting an optimum max cut where after undergoing the cut, separate into two partitions $S = 1, 4$ (blue) and $\bar{S} = 2, 3, 5$ (black). The size of the cut is $f(x) = 5$ and the spin configuration depicted as $x = \{1, -1, -1, 1, -1\}$.

As a result, increasing the interaction strength fourfold leads to a speed-up in reaching the maximum success rate, as depicted in Figure 7(a). We also observe a surprising result: an improvement in the success rate when $J_{coef}(t)$ is increased linearly, as depicted by the green plot in Figure 7(a).

A. Case II: Max-cut problem

In this section, we explore a five-mode Max Cut problem. Max Cut problems are often used to solve flow optimization challenges, where the goal is to calculate the maximum capacity of a network when transferring from one side to the other. These problems have many practical applications [11, 13], ranging from calculating traffic flow to determining the flow of liquids or gases in pipes, among others. Each cut represents a line passing through the network, dividing it into two parts, as illustrated in Figure 8. The cut capacity is the total capacity, or weight, of all edges the cut passes through, calculated by summing the weights of these edges. For simplicity, in this case, we assume uniform weights.

We can map the Max-Cut problem onto our CIM model by setting $J_{ij} < 0$. Here, we fix the initial state as ψ_{vac} and set $J_{coef} = 1$. Instead of varying J_{coef} , we make the non-linear dissipation g in Eq. 7 time-dependent and investigate different strategies for $g(t)$. In this context, we aim to keep α fixed at 2.582. Since the coherent amplitude α depends on g and λ (given by $\alpha = \frac{\sqrt{\lambda}}{g}$), we vary the pump strength λ in conjunction with g , ensuring that α remains constant.

When $g \ll 1$, the system experiences weak quantum noise, remaining in the classical regime. For $g \sim 1$, the system is exposed to sufficiently strong quantum noise,

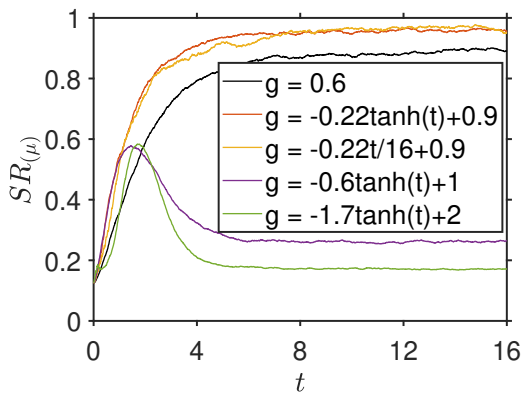


Figure 9: Success rate measurement for the 5 mode Max-cut problem, where we consider differing strategies for non-linear dissipation g . Here $\alpha = 2.582$.

pushing it into the non-classical regime. We observe an improvement in the simulation, specifically an increase in the maximum success rate, when g is varied from 0.9, (a higher non-classical regime) to 0.6 (a lower non-

classical regime), as shown in Figure 9.

V. CONCLUSION

We have demonstrated fully quantum simulations of the Coherent Ising machine, in regimes where quantum effects cannot be neglected. The use of number-state cut-offs well above the mean photon number, together with quantum Monte-Carlo methods, allow careful investigation of quantum effects. We show that dynamical strategies with the coupling changing in time from an initial quantum regime to a final classical regime are beneficial. There is clear potential for enhanced success rates in the quantum regime. However, these studies must be regarded as transitional, in that there are many other dynamical strategies possible. Further results and different strategies will be reported elsewhere.

ACKNOWLEDGMENTS

This research was funded through grants from NTT Phi Laboratories and a Templeton Foundation grant ID 62843.

-
- [1] R. P. Feynman, International Journal of Theoretical Physics **21**, 476 (1982).
 - [2] M. A. Nielsen and I. L. Chuang, *Quantum computation and quantum information* (Cambridge university press, 2010).
 - [3] F. Arute, K. Arya, R. Babbush, D. Bacon, J. C. Bardin, R. Barends, R. Biswas, S. Boixo, F. G. Brandao, D. A. Buell, *et al.*, Nature **574**, 505 (2019).
 - [4] H.-S. Zhong, H. Wang, Y.-H. Deng, M.-C. Chen, L.-C. Peng, Y.-H. Luo, J. Qin, D. Wu, X. Ding, Y. Hu, *et al.*, Science **370**, 1460 (2020).
 - [5] Y. Wu, W.-S. Bao, S. Cao, F. Chen, M.-C. Chen, X. Chen, T.-H. Chung, H. Deng, Y. Du, D. Fan, *et al.*, Physical review letters **127**, 180501 (2021).
 - [6] Q. Zhu, S. Cao, F. Chen, M.-C. Chen, X. Chen, T.-H. Chung, H. Deng, Y. Du, D. Fan, M. Gong, *et al.*, Science bulletin **67**, 240 (2022).
 - [7] L. S. Madsen, F. Laudenbach, M. F. Askarani, F. Rortais, T. Vincent, J. F. Bulmer, F. M. Miatto, L. Neuhaus, L. G. Helt, M. J. Collins, *et al.*, Nature **606**, 75 (2022).
 - [8] P. D. Drummond, B. Opanchuk, A. Delliios, and M. D. Reid, Physical Review A **105**, 012427 (2022).
 - [9] A. J. Daley, I. Bloch, C. Kokail, S. Flannigan, N. Pearson, M. Troyer, and P. Zoller, Nature **607**, 667 (2022).
 - [10] G. F. Newell and E. W. Montroll, Rev. Mod. Phys. **25**, 353 (1953).
 - [11] M. G. Teodor Gabriel Crainic and A. Frangioni, eds., *Combinatorial Optimization and Applications*, Vol. 358 (Springer nature Switzerland, 2024).
 - [12] P. Crescenzi and V. Kann, A compendium of np optimization problems.
 - [13] K. Sankar, A. Scherer, S. Kako, S. Reifenstein, N. Ghadermarzy, W. B. Krayenhoff, Y. Inui, E. Ng, T. Onodera, P. Ronagh, *et al.*, arXiv preprint arXiv:2105.03528 (2021).
 - [14] A. Lucas, Frontiers in Physics **2**, 5 (2014).
 - [15] F. W. Glover and G. A. Kochenberger, ArXiv **abs/1811.11538** (2018).
 - [16] Y. Yamamoto, K. Aihara, T. Leleu, K. I. Kawarabayashi, S. Kako, M. Fejer, K. Inoue, and H. Takesue, Coherent ising machines - optical neural networks operating at the quantum limit (2017).
 - [17] A. Marandi, Z. Wang, K. Takata, R. L. Byer, and Y. Yamamoto, Nature Photonics **8**, 937 (2014).
 - [18] P. L. McMahon, A. Marandi, Y. Haribara, R. Hamerly, C. Langrock, S. Tamate, T. Inagaki, H. Takesue, S. Utsunomiya, K. Aihara, R. L. Byer, M. M. Fejer, H. Mabuchi, and Y. Yamamoto, Science **354**, 614 (2016), <https://www.science.org/doi/pdf/10.1126/science.aah5178>.
 - [19] T. Inagaki, K. Inaba, R. Hamerly, K. Inoue, Y. Yamamoto, and H. Takesue, Nature Photonics **10**, 415 (2016).
 - [20] T. Honjo, T. Sonobe, K. Inaba, T. Inagaki, T. Ikuta, Y. Yamada, T. Kazama, K. Enbutsu, T. Umeki, R. Kasahara, *et al.*, Science advances **7**, eabh0952 (2021).
 - [21] R. Y. Teh, P. D. Drummond, and M. D. Reid, Physical Review Research **2**, 10.1103/PhysRevResearch.2.043387 (2020).
 - [22] S. Kiesewetter and P. D. Drummond, Physical Review A **106**, 10.1103/PhysRevA.106.022409 (2022).
 - [23] P. D. Drummond and C. W. Gardiner, Journal of Physics A: Mathematical and General **13**, 2353 (1980).

- [24] E. Ng, T. Onodera, S. Kako, P. L. McMahon, H. Mabuchi, and Y. Yamamoto, *Physical Review Research* **4**, 10.1103/PhysRevResearch.4.013009 (2022).
- [25] K. Mølmer, Y. Castin, and J. Dalibard, *JOSA B* **10**, 524 (1993).
- [26] P. Drummond, K. McNeil, and D. Walls, *Optica Acta: International Journal of Optics* **27**, 321 (1980).
- [27] P. Drummond, K. McNeil, and D. Walls, *Optica Acta: International Journal of Optics* **28**, 211 (1981).
- [28] P. Kinsler and P. D. Drummond, *Quantum dynamics of the parametric oscillator* (1991).
- [29] H. J. Carmichael, *Statistical methods in quantum optics 2: Non-classical fields* (Springer Science & Business Media, 2009).
- [30] L. Krippner, W. J. Munro, and M. D. Reid, *Physical Review A* **50**, 4330 (1994).
- [31] M. Wolinsky and H. J. Carmichael, *Physical Review Letters* **60**, 1836 (1988).
- [32] L. Gilles, B. M. Garraway, and P. L. Knight, *Physical Review A* **49**, 2785 (1994).
- [33] A. Marandi, Z. Wang, K. Takata, R. L. Byer, and Y. Yamamoto, *Nature Photonics* **8**, 937 (2014).
- [34] H. Goto, *J. Phys. Soc. Jpn.* **88** (2019).
- [35] Y. Inui and Y. Yamamoto, *Physical Review A* **102**, 062419 (2020).
- [36] H. Goto, *Quantum computation based on quantum adiabatic bifurcations of kerr-nonlinear parametric oscillators* (2019).
- [37] K. T. Hayato Goto and A. R. Dixon, *Sci Adv.* **5** (2019).
- [38] C. H. Mingrui Jiang, Keyi Shan and C. Li, *Nature Communications* **14** (2023).
- [39] Y. Haribara, S. Utsunomiya, and Y. Yamamoto, *Entropy* **18**, 10.3390/e18040151 (2016).
- [40] N. Gisin and I. C. Percival, *Journal of Physics A: Mathematical and General* **25**, 5677 (1992).
- [41] F. M.-F. M. Rigo and P. O'Mahony, *Journal of Physics A: Mathematical and General* **30**, 7557 (1997).
- [42] Y. C. K. Mølmer and J. Dalibard, *Journal of the Optical Society of America B* **10**, 524 (1993).
- [43] e. a. Peter D. Drummond, *The quantum and stochastic toolbox: xspde4.2*.
- [44] J. Johansson, P. Nation, and F. Nori, *Computer Physics Communications* **183**, 1760 (2012).
- [45] J. Johansson, P. Nation, and F. Nori, *Computer Physics Communications* **184**, 1234 (2013).
- [46] T. A. B. Kennedy and D. F. Walls, *Physical Review A* **37**, 152 (1988).